Impact of Coordination Environment on Single-atom-embedded C_3N for Oxygen Electrocatalysis

Xiting Wang,[†] Huan Niu,[†] Xuhao Wan,[†] Anyang Wang,[†] Feng Ryan Wang,[‡] and Yuzheng Guo[†,]*

†School of Electrical Engineering and Automation, Wuhan University, Wuhan, Hubei 430072, China

‡Departments of Chemical Engineering, University College London, Torrington Place, London WC1E 7JE, UK

*Corresponding Author.

E-mail address: yguo@whu.edu.cn (Y. Guo)

ABSTRACT

Herein, utilizing density functional theory (DFT) calculations, we have assessed the feasibility of single-atom-embedded C_3N with the various coordination environments of $TM-C_3$, $TM-C_2N_1$, $TM-C_4$, and $TM-C_2N_2$ for oxygen electrocatalysis. It is proved that most $TM-C_xN_y$ candidates are stable and all of them possess metallic features to ensure fast electron transfer. Importantly, $Co-C_2N_2$ is considered as a bifunctional noble-metal-free catalyst with low OER and ORR overpotentials of 0.33 and 0.39 V. Furthermore, the impact of coordination environment on adsorption trend is revealed by the electronic properties for $TM-C_xN_y$. Considering both the number of TM-d orbital electrons and the electronegativity of TM atoms and coordinated C/N atoms, a universal descriptor φ is proposed and offers more understandings to the coordination-activity correlation. Our findings not only show the promising single-atom-embedded C_3N candidates for oxygen electrocatalysis but also deeply unveil the impact of coordination environment on catalytic activity.

INTRODUCTION

Developing sustainable energy technologies is an attractive approach to solve the problem of fossil fuel depletion and environmental pollution.[1, 2] Electrochemical energy conversion strategies, incorporating water electrolysis, fuel cells, and metal-air batteries, have gained great interest with the merits of high efficiency and low emission.[3-6] Oxygen evolution reaction (OER) and oxygen reduction reaction (ORR) play a key role in these advanced technologies.[7, 8] Noble-metal-based Ru/Ir oxide and Pt have been known as efficient catalysts for OER and ORR, respectively.[9-11] Nevertheless, their widespread applications are hindered by the high cost and poor stability of these noble metals.[12] Accordingly, it is desirable to minimize or completely replace the usage of noble metals and maintain the comparable activity for the design of OER and ORR catalysts.[13]

The emerging single-atom catalysts (SACs) have attracted extensive attention with the isolated transition metal (TM) atoms anchored on substrates.[14-16] The high atomic utilization of SACs results in minimized metal usage, especially beneficial for noble metal-based catalysts.[17, 18] Moreover, SACs exert outstanding catalytic performance, high selectivity, and long-time stability, compared with metal nanoparticle catalysts.[19, 20] Owing to these features, SACs have been demonstrated as promising catalysts for various electrochemical reactions in both theoretical and experimental studies.[20-23] However, the single metal atoms would easily aggregate into clusters due to the high surface free energy.[24, 25] Two-dimensional (2D) materials, such as N-doped graphene,[26-28] graphitic carbon nitride,[29-31] Mxenes,[32, 33] and transition metal dichalcogenides,[34, 35]

have become the distinguished substrates to firmly anchor SACs owing to the large surface area and high stability. For example, the metal-nitrogen-carbon (M-N-C) materials such as Fe-N-C have been considered as outstanding catalysts for ORR.[36-38]

Recently, a novel 2D-layered polyaniline framework with the formula of C_3N has been synthesized via the direct pyrolysis of hexaaminobenzene trihydrochloride single crystals.[39] The intrinsic electronic, mechanical, and chemical properties of C_3N have been intensively explored.[40, 41] It is predicted that C_3N shows the prospects in metal-ion batteries, gas sensors, gas capture, and catalysis.[42-45] Particularly, the C_3N framework can serve as a suitable support for SACs to achieve superior electrocatalytic performance.[45-47] The single or double C/N vacancies should be introduced to the hole-free C_3N plane for stabilizing SACs. In this regard, the TM atoms can be embedded in C_3N with diverse coordinated C and N atoms, forming the $TM-C_xN_y$ configurations. It is well-known that coordination engineering can effectively modulate the catalytic performance. Therefore, unveiling the effect of the coordination environment for C_3N-supported SACs is an intriguing task, which can promote the understanding of the structure-activity relation and guide the design of highly active catalysts.

In this study, we have systematically evaluated the stability, electronic properties, and OER/ORR activity for $TM-C_xN_y$ (including $TM-C_3$, $TM-C_2N_1$, $TM-C_4$, and $TM-C_2N_2$). It was demonstrated that $Co-C_2N_2$ exhibited the low overpotentials of 0.33 and 0.39 V for OER and ORR, respectively, and thus was considered as bifunctional OER/ORR catalysts. The OER/ORR volcano plots and the OER/ORR polarization curves were drawn to further clarify the superior performance of catalysts. The

electronic properties of TM-C_xN_y were analyzed to shed light on the impact of different coordination environments on catalytic activity. Moreover, a series of descriptors were examined to rationally explain the OER/ORR activity origin on TM-C_xN_y. The discovery of the universal descriptor φ can provide guidance for the design and optimization of SACs.

COMPUTATIONAL METHODS

All first-principles calculations were carried out based on spin-polarized density functional theory (DFT) methods, as implemented in the Vienna Ab initio Simulation Package.[48] We adopted the projector augmented wave (PAW) method to describe the interaction between valance and core electrons. The exchange-correlation energy was treated by generalized gradient approximation (GGA) in the form of Perdew-Burke-Ernzerhof (PBE) functional.[49] The HSE06 functional calculations were utilized to depict the band structures of pristine C_3N.[50] The first Brillouin zone was sampled with the 3×3×1 Monkhorst-Pack k-point grid for structural optimization and a denser 7×7×1 sampling grid was adopted for electronic properties. All configurations were fully optimized until energy and force change within 10^{-5} eV and 0.02 eV/Å, respectively. The vacuum gap of 20 Å along the z-direction was applied to avoid the interactions between two adjacent layers under periodic boundary conditions. The van der Waals interactions were described by Grimme's DFT-D3 scheme.[51] Considering the solvation effect can enhance the adsorption energy (**Table S1**), the implicit solvent model VASPsol was included with a dielectric constant of 78.4.[52] The energy barriers of the OER/ORR process were computed by using the climbing-image nudged elastic band

(CI-NEB) method[53]. The convergence criterion of force was set to 0.05 eV Å^{-1} during CI-NEB calculations.

The Gibbs free energy change (ΔG) of OER/ORR elementary step can be calculated as[54, 55]

$$\Delta G = \Delta E + \Delta ZPE - T\Delta S + \Delta U \tag{1}$$

where ΔE denotes the total energy change. ΔZPE and ΔS represent the zero-point energy and entropy corrections at 298.15 K, respectively (details in **Table S2**). The effect of the applied potential is considered in $\Delta U = -eU$, in which e and U are the number of transferred electrons and the applied potential, respectively.

To evaluate the catalytic activity, the OER and ORR overpotentials (η) are calculated as

$$\eta_{OER} = \Delta G_{max} / e - 1.23 \tag{2}$$

$$\eta_{ORR} = 1.23 - \Delta G_{max'} / e \tag{3}$$

where ΔG_{max} and $\Delta G_{max'}$ are the free energy changes of the most difficult step in the whole OER and ORR reaction, which is called the potential-determining step (PDS). More details for the OER/ORR activity evaluation are given in the supporting information.

RESULTS AND DISCUSSION

Structure, stability, and electronic property

As shown in **Figure 1a**, the primitive cell of pristine C_3N is composed of six carbon atoms and two nitrogen atoms with the lattice parameter of 4.86 Å. The (3×3) C_3N supercell is adopted for further calculations, as presented in **Figure S1**. The

extended C_3N plane shows the graphene-like honeycomb structure with similar C-C and C-N bond lengths of 1.40 Å. Two kinds of single vacancies (SV: V_C and V_N) and two kinds of double vacancies (DV: V_{CC} and V_{CN}) can be formed on pristine C_3N. The configurations of the defective C_3N can be seen in **Figure S1**. To assess the formation possibility of V_C, V_N, V_{CC}, and V_{CN} in C_3N, the vacancy formation energies (E_{vf}) are calculated as

$$E_{vf} = E_V - E_P + \mu_{C/N} \tag{4}$$

where E_V and E_P are the total energies of the defective C_3N and pristine C_3N, respectively. $\mu_{C/N}$ is the chemical potential of the carbon or nitrogen atom, which denotes the total energy of per C atom in graphene or per N atom in the N_2 molecule, respectively. The E_{vf} values for V_C, V_N, V_{CC}, and V_{CN} are 4.61, 4.82, 4.83, and 6.71 eV, respectively. For comparison, the vacancy formation energies of SV and DV in graphene are calculated as 8.09 and 8.20 eV, respectively. The lower E_{vf} values of defective C_3N suggest the thermodynamically favorable formation of vacancies on C_3N.

The diverse forms of vacancies on the C_3N plane can provide different coordination environments for SACs. Specifically, the TM atoms can be embedded in V_C, V_N, V_{CC}, and V_{CN}, forming the structures of TM-C_2N_1, TM-C_3, TM-C_2N_2, and TM-C_4, respectively (**Figure 1a**). Ten TM atoms are investigated in this work (TM=Fe, Co, Ni, Cu, Ru, Rh, Pd, Ag, Ir, and Pt). All TM-C_xN_y configurations embedded in C_3N are presented in **Figure S2-S5.** The details of bond lengths and magnetic moments for TM-C_xN_y configurations are listed in **Table S3-S6**. Notably, the TM atoms in TM-C_2N_1 and TM-C_3 prefer to protrude the C_3N plane, while TM-C_2N_2 and TM-C_4 can maintain
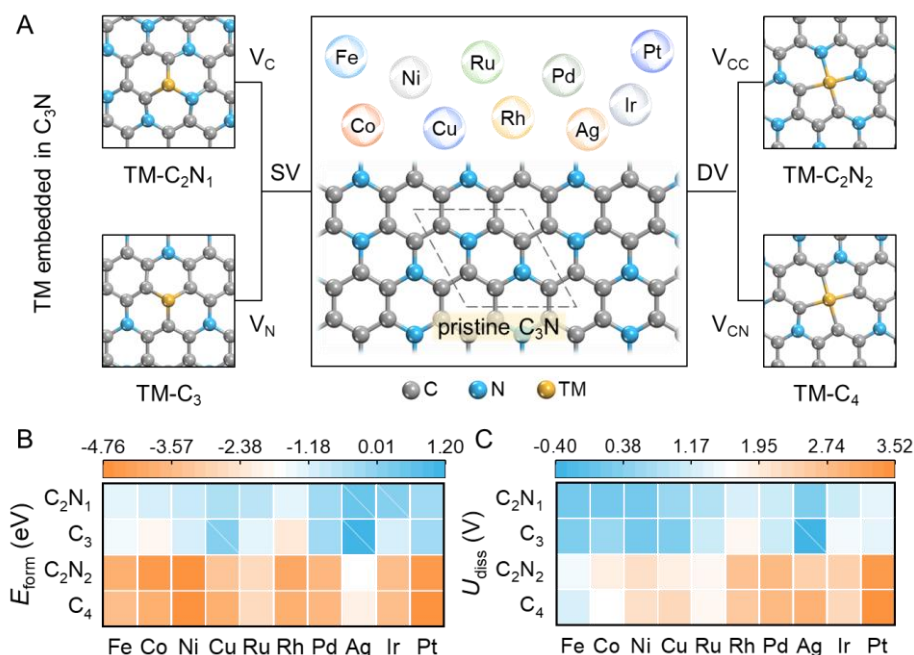
planar structures.

Figure 1. (a) Configurations of pristine C_3N and TM-embedded C_3N. The TM atoms can be anchored at single vacancies (SV: V_C and V_N) and double vacancies (DV: V_{CC} and V_{CN}) on C_3N with the moiety of TM-C_xN_y (TM-C_2N_1, TM-C_3, TM-C_2N_2, and TM-C_4). The heatmaps of (b) formation energies (E_{form}) and (c) dissolution potentials (U_{diss}) for TM-C_xN_y configurations.

To prove the thermodynamic stability, the formation energy (E_{form}) is calculated as

$$E_{form} = E_{TM\text{-}C3N} - E_{V\text{-}C3N} - E_{TM} \tag{5}$$

where $E_{TM\text{-}C3N}$, $E_{V\text{-}C3N}$, and E_{TM} denote the total energies of TM-embedded C_3N, defective C_3N, and TM atom in bulk, respectively. The criterion of $E_{form} < 0$ should be satisfied for a thermodynamically stable TM-C_xN_y configuration. The heatmap of E_{form} values for all TM-C_xN_y configurations is plotted in **Figure 1b** and the detailed formation energies are summarized in **Table S7**. It is indicated that TM-C_2N_2 and TM-C_4 exhibit the more negative E_{form} and thus are more thermodynamically stable than

TM-C_2N_1 and TM-C_3. In addition, most TM-C_xN_y candidates are stable without the risk of aggregation, except for Ag-C_2N_1, Ir-C_2N_1, Cu-C_3, and Ag-C_3. Besides, considering the formation process of TM-C_xN_y relative to pristine C_3N, the $E_{vf} + E_{form}$ values are calculated as listed in **Table S8**. Similarly, TM atoms embedded in DV-C_3N exert lower $E_{vf} + E_{form}$ values and thus show higher stability than those embedded in SV-C_3N.

Moreover, to investigate the electrochemical stability, the dissolution potential (U_{diss}) is defined as

$$U_{diss} = U_{diss'} - E_{form}/(n_e e) \qquad (6)$$

in which $U_{diss'}$ denotes the standard dissolution potential for TM in the bulk phase and n_e represents the number of transferred electrons during dissolution. The positive dissolution potential ($U_{diss} > 0$) means the stable TM-C_xN_y structure under electrochemical conditions.[56] The heatmap of U_{diss} values for TM-C_xN_y systems is plotted in **Figure 1c** and the detailed U_{diss} values are listed in **Table S9-S12**. The calculated results prove that TM-C_2N_2 and TM-C_4 are more electrochemically stable with more positive U_{diss} values, compared with TM-C_2N_1 and TM-C_3. The dissolution potentials for almost all TM-C_xN_y configurations are positive, except for Ag-C_3. Note that the unstable configurations (Ag-C_2N_1, Ir-C_2N_1, Cu-C_3, and Ag-C_3) are still remained in the following discussion to guarantee sufficient samples for the analysis of OER/ORR trend and the design of universal descriptor.

Electrical conductivity is an essential factor to assess electrocatalytic activity. The superior electrical conductivity can guarantee the fast charge transfer during OER and ORR.[57] **Figure S6** shows the electronic band structures of pristine C_3N, revealing

the C_3N is a semiconductor with the bandgap of 1.04 eV at the HSE06 level, in line with the previous report.[58] The semiconducting properties prohibit electrochemical applications of C_3N. After embedding TM atoms, TM-C_xN_y candidates show metallic properties. The total density of states (TDOS) for all TM-C_xN_y configurations are presented in **Figure S7-S10**. It is found that electronic states distribute across the Fermi level for all TM-C_xN_y systems, proving the outstanding electronic conductivity.
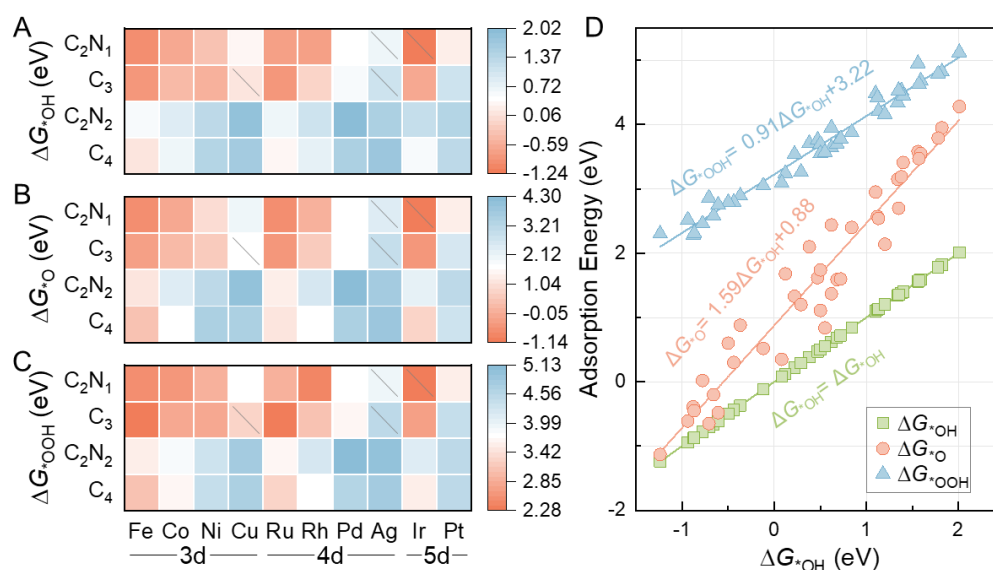
OER/ORR performance

Figure 2. The adsorption energies of (a) *OH, (b) *O, and (c) *OOH (ΔG_{*OH}, ΔG_{*O}, and ΔG_{*OOH}) for TM-C_xN_y configurations. (d) The scaling relations among ΔG_{*OH}, ΔG_{*O}, and ΔG_{*OOH} on TM-C_xN_y.

The OER and ORR activity highly correlate with the adsorption of *OH, *O, and *OOH. The configurations of *OH, *O, and *OOH intermediates adsorbed on TM-C_xN_y are fully relaxed (**Figure S11-S14**) to analyze adsorption energies of *OH, *O, and *OOH (ΔG_{*OH}, ΔG_{*O}, and ΔG_{*OOH}). Similar trends of *OH, *O, and *OOH

adsorption variation on different TM-C_xN_y moieties are observed in **Figure 2a-c**. The adsorption energies of OER/ORR intermediates gradually get weaker from left to right in a row. For example, the ΔG_{*OH} values for Fe-C_2N_1, Co-C_2N_1, Ni-C_2N_1, and Cu-C_2N_1 are -0.94, -0.66, -0.37, 0.38 eV, respectively. Additionally, the adsorption strength of intermediates on TM-C_2N_1 and TM-C_3 is much stronger than that on TM-C_2N_2 and TM-C_4, suggesting the significant effect of coordination environment on adsorption behavior. The detailed ΔG_{*OH}, ΔG_{*O}, and ΔG_{*OOH} values are listed in **Table S13-S16**. Moreover, the formation of similar TM-O bonds when intermediates (*OH, *O, and *OOH) adsorbed on TM-C_xN_y leads to the scaling relations among ΔG_{*OH}, ΔG_{*O}, and ΔG_{*OOH} (**Figure 2d**). In this regard, ΔG_{*O} and ΔG_{*OOH} can be expressed as $\Delta G_{*O} = 1.59\Delta G_{*OH} +0.88$ and $\Delta G_{*OOH} = 0.91\Delta G_{*OH} + 3.22$. Therefore, the OER/ORR activity volcano can be drawn based on the linear scaling relations among ΔG_{*OH}, ΔG_{*O}, and ΔG_{*OOH}, which will be discussed later.
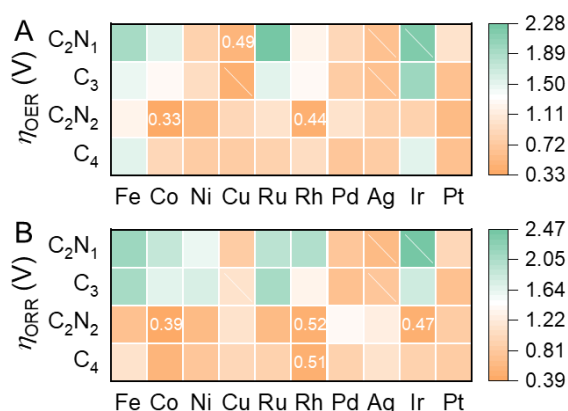

Figure 3. The heatmaps of (a) OER and (b) ORR overpotentials (η_{OER} and η_{ORR}) for TM-C_xN_y.

We then calculate the free energy change of each OER/ORR elementary step, as summarized in **Table S17-S20**. The OER and ORR overpotentials (η_{OER} and η_{ORR}) for

all TM-C_xN_y candidates can be seen in **Figure 3** (detail values in **Table S21**).

Encouragingly, Cu-C_2N_1, Co-C_2N_2, and Rh-C_2N_2 exhibit outstanding OER

performance with the η_{OER} of 0.49, 0.33, and 0.44 V, respectively, which are comparable

to RuO_2 (η_{OER}=0.42 V).[59] Moreover, Co-C_2N_2, Rh-C_2N_2, Ir-C_2N_2, and Rh-C_4 possess

superior ORR performance with the η_{ORR} of 0.39, 0.52, 0.47, and 0.51 V, respectively.

The four candidates are expected to show comparable ORR activity to Pt(111)

(η_{ORR}=0.45 V).[54] Particularly, Co-C_2N_2 and Rh-C_2N_2 can serve as bifunctional

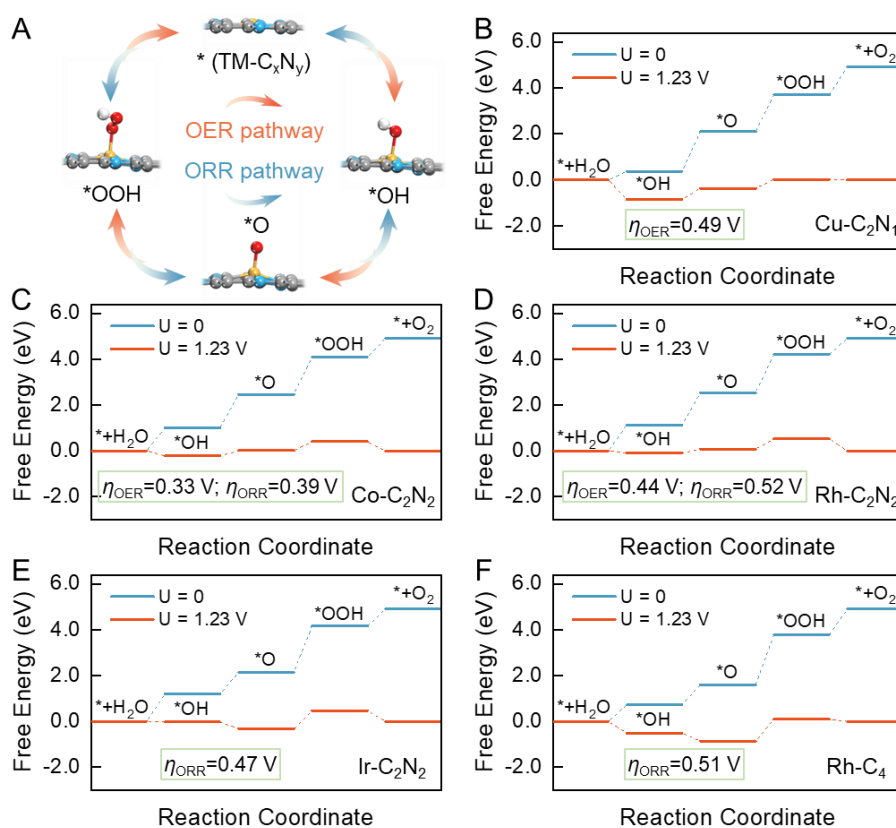OER/ORR catalysts and simultaneously drive OER and ORR.

Figure 4. (a) The OER and ORR pathway on TM-C_xN_y. The OER/ORR free energy

diagrams for (b) Cu-C_2N_1, (c) Co-C_2N_2, (d) Rh-C_2N_2, (e) Ir-C_2N_2, and (f) Rh-C_4,

respectively. The applied potential is set to 0 and 1.23 V, respectively. The OER process

is from left to right, while the ORR process is reversed.

Figure 4a presents the illustration of the OER and ORR pathway on TM-C_xN_y. The OER pathway includes four elementary steps in acid conditions with the process of *+H_2O→*OH→*O→*OOH→*+O_2, while the ORR is the reversed reaction of OER. The OER/ORR free energy diagrams for Cu-C_2N_1, Co-C_2N_2, Rh-C_2N_2, Ir-C_2N_2, and Rh-C_4 are plotted in **Figure 4b-f**. It is seen that all OER elementary steps are endothermic without applied potential. When the equilibrium potential of 1.23 V is applied, more energy input is still required to overcome the PDS. The PDS of the OER process is the second step (*OH → *O) on Cu-C_2N_1 (1.72 eV) and Co-C_2N_2 (1.56 eV), while the OER process is limited by the third step (*O → *OOH) on Rh-C_2N_2 (1.67 eV). As for the ORR process, the PDS is the fourth step (*OH → *+H_2O) on Co-C_2N_2 (-0.84 eV) and Rh-C_4 (-0.72 eV). The first ORR elementary step (*+O_2 → *OOH) becomes PDS on Rh-C_2N_2 (-0.71 eV) and Ir-C_2N_2 (-0.76 eV). The mild free energy changes of PDS on Cu-C_2N_1, Co-C_2N_2, Rh-C_2N_2, Ir-C_2N_2, and Rh-C_4 result in their low OER/ORR overpotentials. The OER/ORR free energy diagrams for the other TM-C_xN_y candidates can be found in **Figure S15-S18**.
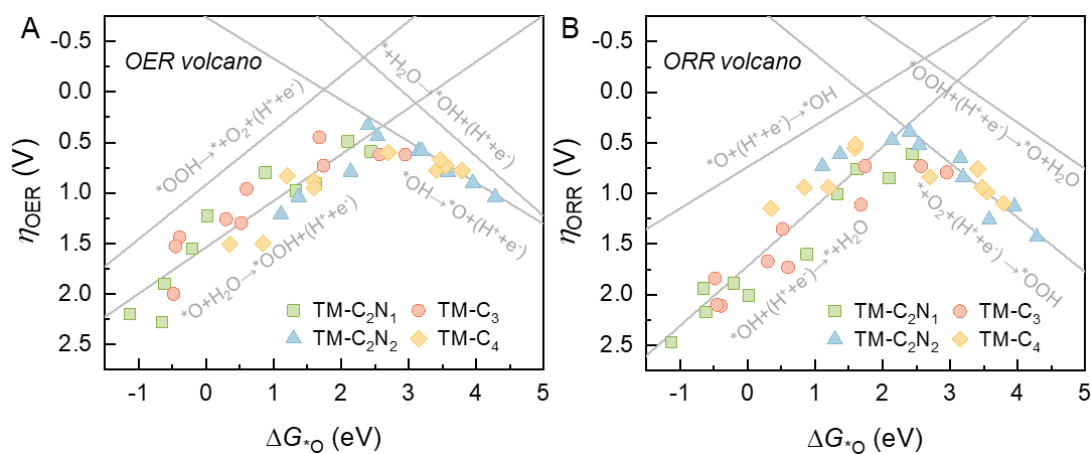

Figure 5. (a) OER and (b) ORR volcano plots (η_{OER} *vs.* ΔG_{*O} and η_{ORR} *vs.* ΔG_{*O}) for TM-C_xN_y established by the scaling relations among ΔG_{*OH}, ΔG_{*O}, and ΔG_{*OOH}. The

solid lines represent the OER/ ORR elementary steps on TM-C_xN_y.

According to the scaling relations among ΔG_{*OH}, ΔG_{*O}, and ΔG_{*OOH} discussed in **Figure 2d**, the adsorption energy of intermediates (*e.g.* ΔG_{*O}) can be the onefold descriptor to reveal OER and ORR activity trend. **Figure 5** presents the OER and ORR volcano plots, which are established by the volcano-shaped relationship between η_{OER} and ΔG_{*O}, as well as between η_{ORR} and ΔG_{*O}. The solid lines represent the OER/ ORR elementary steps on TM-C_xN_y. It is indicated in **Figure 5a** that the OER process is impeded by the step from *O to *OOH when the adsorption is too strong, while the process of *OH → *O becomes PDS for OER when the adsorption is too weak. The ORR volcano plot in **Figure 5b** suggests that the steps of *OH → *+H_2O and *O_2 → *OOH are the main PDS for ORR.

Based on the Sabatier principle,[60] the too weak or too strong binding of intermediates prohibits the adsorption or desorption, respectively, leading to the poor OER/ORR activity. The too strong adsorption of *O on TM-C_2N_1 and TM-C_3 accounts for the sluggish OER and ORR. On the contrary, TM-C_2N_2 and TM-C_4 show more efficient OER/ORR activity owing to the moderate adsorption strength. The OER volcano peak corresponds to the ΔG_{*O} of around 2.60 eV and the best ORR catalysts approximately possess the ΔG_{*O} of 2.40 eV. The promising OER catalysts (Cu-C_2N_1, Co-C_2N_2, and Rh-C_2N_2) locate near the OER volcano peak with the moderate ΔG_{*O}. Co-C_2N_2, Rh-C_2N_2, Ir-C_2N_2, and Rh-C_4 stand near the ORR volcano peak and are considered desirable ORR catalysts. Especially, Co-C_2N_2 and Rh-C_2N_2 possess ΔG_{*O} of 2.40 and 2.54 eV and exhibit bifunctional OER/ORR activity with the η_{OER}/η_{ORR} of

0.33/0.39 and 0.44/0.52 V, respectively. The sum of OER and ORR overpotentials ($\eta_{OER}+\eta_{ORR}$) for Co-C$_2$N$_2$ and Rh-C$_2$N$_2$ is calculated, as seen in **Table S22**. It is indicated that Co-C$_2$N$_2$ can serve as a superior OER/ORR catalyst with a low $\eta_{OER}+\eta_{ORR}$ value, compared with other reported catalysts.

Moreover, to clarify the OER/ORR kinetic feasibility of Co-C$_2$N$_2$, we perform CI-NEB calculations and analyze the kinetic energy barriers. The configurations of initial states (IS), transition states (TS), and final states (FS) during the OER/ORR process are presented in **Figure S19**. It can be found that the second step (from *OH to *O) is the OER rate-determining step (RDS) on Co-C$_2$N$_2$, with the largest energy barrier of 1.80 eV. As for the ORR process, the fourth step (from *OH to *+H$_2$O) exhibits the highest barriers of 0.60 eV and thus becomes the RDS of ORR. Therefore, these results suggest that the most difficult OER/ORR thermodynamic step on Co-C$_2$N$_2$ also possesses the highest kinetic energy barrier.
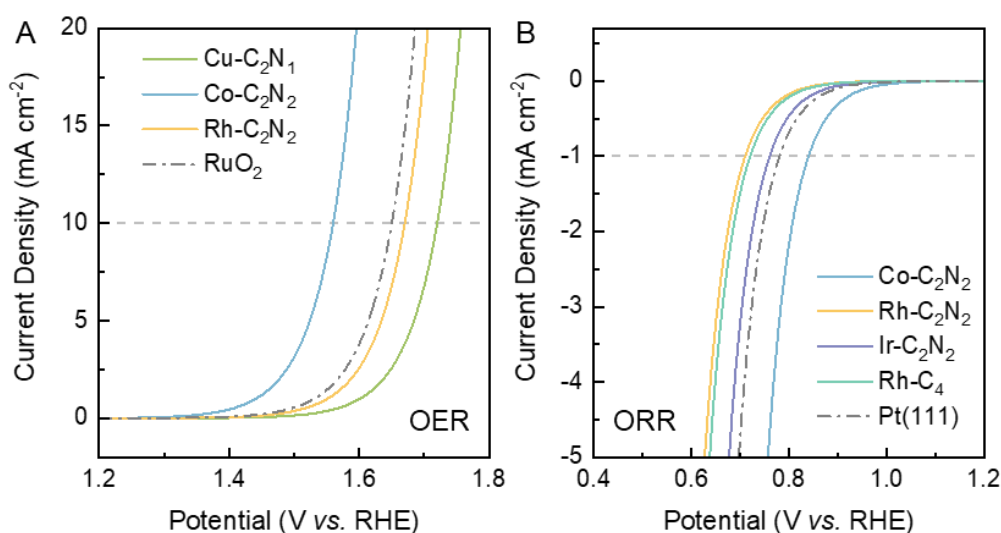

Figure 6. (a) The theoretical OER polarization curves for Cu-C$_2$N$_1$, Co-C$_2$N$_2$, and Rh-C$_2$N$_2$ compared with that of RuO$_2$. (b) The theoretical ORR polarization curves for Co-C$_2$N$_2$, Rh-C$_2$N$_2$, Ir-C$_2$N$_2$, and Rh-C$_4$ compared with that of Pt(111).

To elucidate the OER and ORR activity in practice, we simulate the OER polarization curves for Cu-C$_2$N$_1$, Co-C$_2$N$_2$, and Rh-C$_2$N$_2$, as well as the ORR polarization curves for Co-C$_2$N$_2$, Rh-C$_2$N$_2$, Ir-C$_2$N$_2$, and Rh-C$_4$. The benchmarks for OER and ORR are chosen as RuO$_2$ and Pt(111), respectively. This simulated method has been developed and applied to theoretically visualize the OER and ORR performance, filling the gap between the calculated and experimental results (details in the supporting information).[61-63] As plotted in **Figure 6a**, the OER onset potentials (U_{OER} at the current density of 10 mA·cm^{-2}) are 1.72, 1.57, and 1.67 V for Cu-C$_2$N$_1$, Co-C$_2$N$_2$, and Rh-C$_2$N$_2$, respectively. **Figure 6b** presents that Co-C$_2$N$_2$, Rh-C$_2$N$_2$, Ir-C$_2$N$_2$, and Rh-C$_4$ exert the ORR onset potentials (U_{ORR} at the current density of 1 mA·cm^{-2}) of 0.84, 0.71, 0.76, and 0.72 V, respectively. Compared with the U_{OER} (1.65 V) for RuO$_2$ and U_{ORR} (0.78 V) for Pt(111), Co-C$_2$N$_2$ exhibits better catalytic performance for both OER and ORR and serves as promising noble-free SACs for oxygen electrocatalysis.
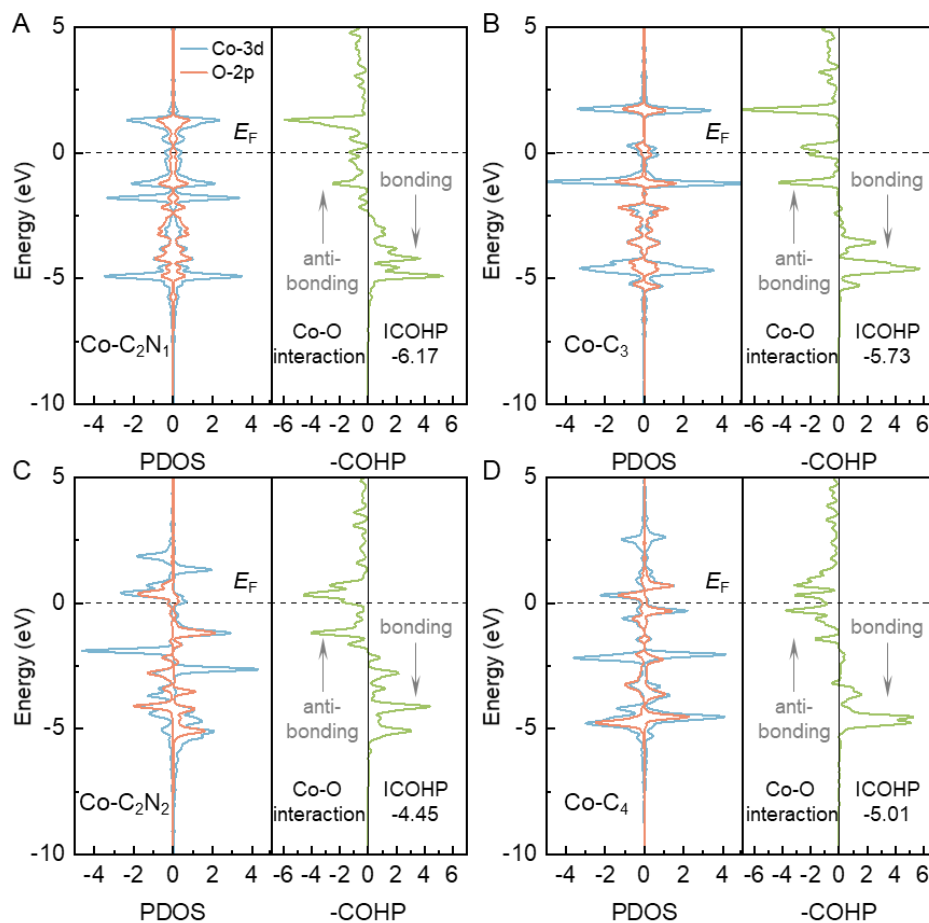
OER/ORR activity origin

Figure 7. Partial density of states (PDOS) and projected crystal orbital Hamilton population (pCOHP) for *O adsorbed on (a) Co-C_2N_1, (b) Co-C_3, (c) Co-C_2N_2, and (d) Co-C_4. The interaction between Co-3d and O-2p orbitals in the PDOS and pCOHP are analyzed. The bonding and antibonding states in pCOHP are drawn on the right and left sides, respectively. The Fermi level (E_F) is set to 0 eV.

The partial density of states (PDOS) and projected crystal orbital Hamilton population (pCOHP) for *O adsorbed on Co-C_xN_y are analyzed to better unveil the effect of different coordination environments. The significant hybridization between Co-3d and O-2p orbitals can be found in **Figure 7a-d**. The bonding states of the Co-O

17

interaction are mainly located at -5~-3 eV and antibonding states distribute above -2 eV. Notably, the clear peaks of the unoccupied antibonding states are detected at around +2 eV for *O adsorbed on Co-C_2N_1 and Co-C_3 (**Figure 7a-b**). However, similar peaks are not observed in **Figure 7c-d**. Moreover, the integrated COHP (ICOHP) values are obtained by integrating the energy up to E_F, which can provide a more quantitative explanation. As shown in **Figure S20**, ICOHP linearly correlates with ΔG_{*O}. The more negative ICOHP value indicates the stronger TM-O interaction. The ICOHP values for Co-O interaction on Co-C_2N_1, Co-C_3, Co-C_2N_2, and Co-C_4 are -6.17, -5.73, -4.45, and -5.01, respectively. Thus, compared with DV-C_3N supported SACs (*e.g.* Co-C_2N_2 and Co-C_4), the SACs in SV-C_3N (*e.g.* Co-C_2N_1 and Co-C_3) possess stronger adsorption for intermediates due to the larger proportion of unoccupied antibonding states and more negative ICOHP values. Particularly, Co-C_2N_2 possesses the most moderate Co-O interaction and thus exhibits the best OER/ORR activity (**Figure S21**). On the contrary, Co-C_2N_1, Co-C_3, and Co-C_4 suffer from too strong Co-O interaction and show poor OER/ORR activity.

We then focus on finding suitable descriptors to reveal the variation trend of adsorption strength on TM-C_xN_y. The elements of TM atoms are expanded with the range from Ti to Au, which is beneficial to explore correlations between descriptors and adsorption strength in a broader set of samples. The detailed values for the considered descriptors and the corresponding ΔG_{*O} values on TM-C_xN_y are summarized in **Table S23-S26**. Given that the key role of TM-d orbitals in the adsorption of intermediates, the d-band centers (ε_d) of TM-C_xN_y and the number of TM-d orbital electrons (N_d) are

firstly considered as promising descriptors. **Figure 8a-b** shows the relationships between ε_d and ΔG_{*O}, as well as between N_d and ΔG_{*O}. Both ε_d and N_d correlate linearly with ΔG_{*O} for every single TM-C_xN_y system, exhibiting the correlation coefficient (R^2) of 0.71~0.83 and 0.91~0.93, respectively. Moreover, considering the electronegativity of TM atoms (E_{TM}), the number of TM-d orbital electrons multiplied by the electronegativity of TM atoms ($N_d \times E_{TM}$) is further created as a modified descriptor. **Figure 8c** indicates that $N_d \times E_{TM}$ descriptor is also related to ΔG_{*O} (R^2=0.84~0.88). Whereas, it is noted that the three descriptors (ε_d, N_d, and $N_d \times E_{TM}$) fail to reflect the overall adsorption variation trend for all TM-C_xN_y systems. This is because the diverse coordination environments of TM-C_xN_y can effectively influence the intermediates adsorption (demonstrated in **Figure 7**). However, the three descriptors just simply consider the effect of TM atoms but neglect the effect of coordination environments.
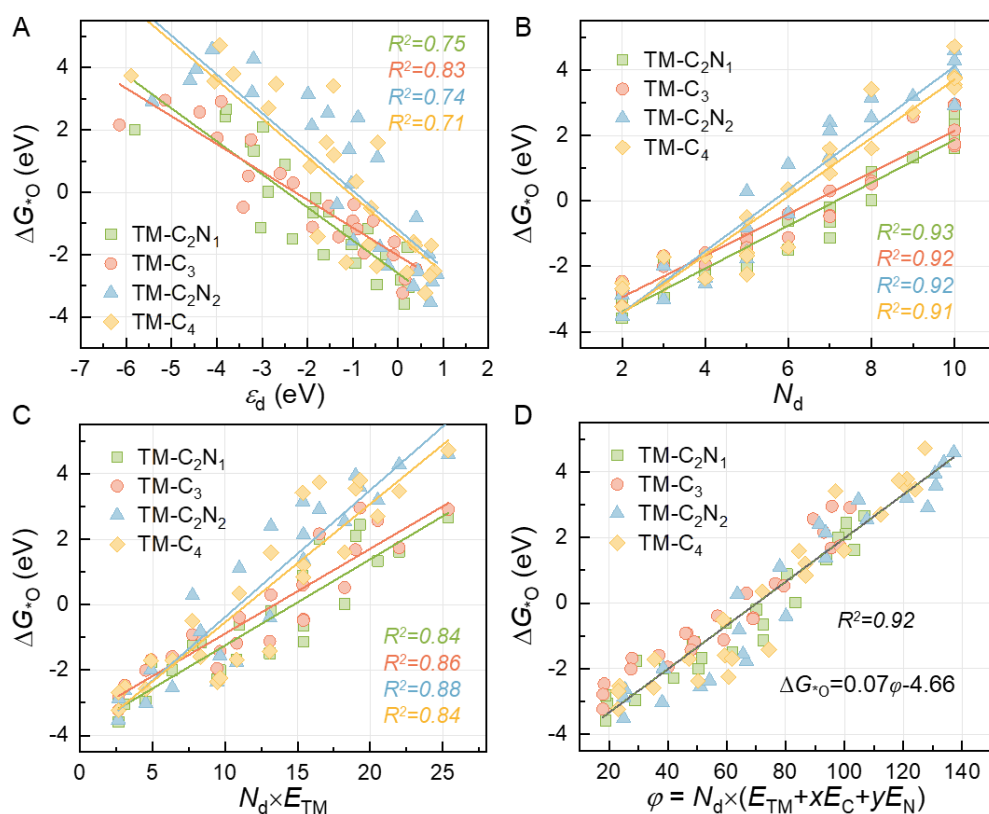
Figure 8. The correlations between the possible descriptors and ΔG_{*O}. The descriptors are considered as (a) d-band center (ε_d), (b) the number of TM-d orbital electrons (N_d), (c) the number of TM-d orbital electrons multiplied by the electronegativity of TM atoms ($N_d \times E_{TM}$), and (d) the number of TM-d orbital electrons multiplied by the electronegativity of TM atoms and coordinated C/N atoms ($\varphi = N_d \times (E_{TM} + xE_C + yE_N)$).
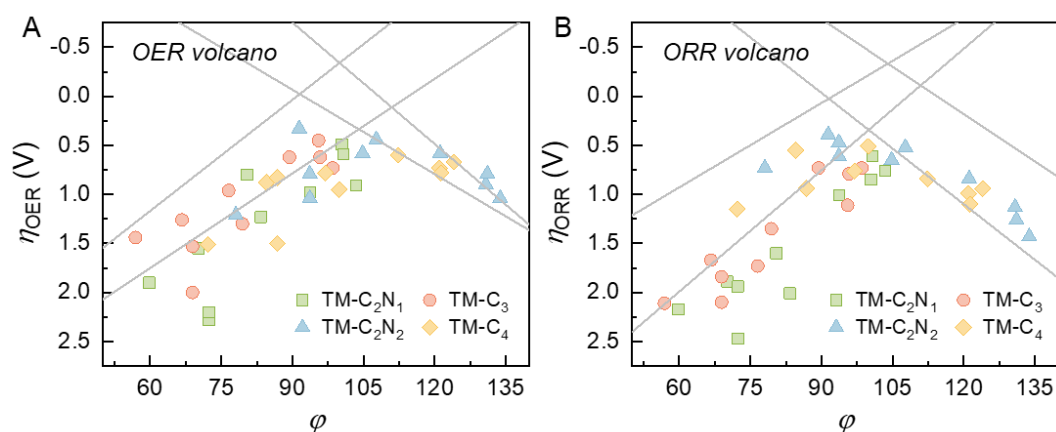

Figure 9. (a) OER and (b) ORR volcano plots (η_{OER} *vs.* φ and η_{ORR} *vs.* φ) for TM-C_xN_y established by the linear relationship between φ and ΔG_{*O}. The solid lines represent the OER/ ORR elementary steps on TM-C_xN_y.

Inspired by the recent studies on the universal descriptors for structure-activity correlation,[16, 64, 65] the intrinsic descriptor (φ) is defined as

$$\varphi = N_d \times (E_{TM} + xE_C + yE_N) \tag{7}$$

where $E_{C/N}$ and x/y refer to the electronegativity and number of coordinated C/N atoms, respectively. As presented in **Figure 8d**, φ correlates with ΔG_{*O} for all TM-C_xN_y systems, which can be fitted as ΔG_{*O}=0.07φ-4.66 (R^2=0.92). The linear relationship between φ and ΔG_{*O} suggests that the larger φ value corresponds to the weaker adsorption strength. Furthermore, using the simple descriptor φ to replace ΔG_{*O} in **Figure 5**, we can derive OER and ORR volcano plots for η_{OER} and η_{ORR} versus φ, as

shown in **Figure 9**. It can be found that the too small or too large φ value will lead to relatively high OER and ORR overpotentials. The optimal φ values for OER and ORR are 104 and 100, respectively. Nevertheless, most TM-C_xN_y candidates exert too small φ value and suffer from the too strong adsorption of intermediates. Based on the definition of φ, we can be guided to rationally tune the φ value and adjust the adsorption strength of intermediates. Taking Fe-C_2N_2 (too strong adsorption of *O, 1.11 eV) as an example, the following strategies can be adopted to improve φ value and weaken the adsorption strength (**Figure S22**): (1) Replacing the TM active site to the late TM atoms with more d orbital electrons. Co-C_2N_2 possesses a larger φ value than Fe-C_2N_2 and exhibits weaker adsorption of *O (2.40 eV). (2) Introducing the coordinated atoms with larger electronegativity, such as O or F. The *O adsorption strength on Fe-$C_1N_2O_1$ and Fe-$C_2N_1O_2$ configurations can be weakened to be 1.27 and 1.35 eV, respectively. (3) Adding axial ligands for SACs to form a higher coordinate structure. Fe-C_2N_2 with the added OH axial ligand shows the ΔG_{*O} of 2.24 eV. Therefore, it is concluded that the descriptor φ can provide the universal explanation to OER/ORR activity origin and show guidance for the discovery of efficient catalysts.

CONCLUSIONS

In summary, we have conducted comprehensive first-principles calculations to investigate the prospects of single-atom-embedded C_3N with the coordination environment of TM-C_xN_y for electrocatalytic OER and ORR. Compared with TM-C_2N_1 and TM-C_3, the configurations of TM-C_2N_2 and TM-C_4 are more thermodynamically and electrochemically stable, and exert weaker bindings for OER/ORR intermediates.

Among all TM-C_xN_y candidates, Cu-C_2N_1, Co-C_2N_2, and Rh-C_2N_2 are promising OER catalysts with the η_{OER} of 0.49, 0.33, and 0.44 V, respectively. Co-C_2N_2 (η_{ORR}=0.39 V), Rh-C_2N_2 (η_{ORR}=0.52 V), Ir-C_2N_2 (η_{ORR}=0.47 V), and Rh-C_4 (η_{ORR}=0.51 V) exhibit superior ORR activity. Notably, both Co-C_2N_2 and Rh-C_2N_2 can simultaneously drive the process of OER and ORR and serve as bifunctional OER/ORR catalysts. Moreover, we have analyzed the electronic properties of TM-C_xN_y to reveal the impact of different coordination environments on OER/ORR activity origin. Furthermore, it is validated that φ is an intrinsic and universal descriptor to unveil the coordination-activity correlation for single-atom-embedded C_3N with TM-C_xN_y configurations. This work not only develops the outstanding C_3N-supported SACs for oxygen electrocatalysis but also offers insights into the effect of coordination environment on OER/ORR activity. We hope this work can facilitate the discovery of advanced SACs.

ASSOCIATED CONTENT

Supporting Information

The Supporting Information is available free of charge at http://pubs.acs.org.

OER/ORR activity evaluation; OER/ORR polarization curve simulation; Adsorption energies with solvation effect; Zero-point energies and entropies; Configurations of pristine/defective C_3N and TM-C_xN_y; Bond lengths and magnetic moments; Formation energies and dissolution potentials; Band structures and density of states; Configurations of intermediates adsorbed on TM-C_xN_y; Adsorption energies of *OH, *O, and *OOH; OER/ORR free energy changes, overpotentials, and free

energy diagrams; OER/ORR kinetic energy barriers on Co-C_2N_2; Correlation between ICOHP and ΔG_{*O}; Descriptors (ε_d, N_d, $N_d \times E_{TM}$, and φ) for TM-C_xN_y; Strategies for improving φ value and weakening the adsorption strength (PDF)

AUTHOR INFORMATION

Corresponding Author

Yuzheng Guo - School of Electrical Engineering and Automation, Wuhan University, Wuhan, Hubei 430072, China; E-mail: yguo@whu.edu.cn

Authors

Xiting Wang - School of Electrical Engineering and Automation, Wuhan University, Wuhan, Hubei 430072, China

Huan Niu - School of Electrical Engineering and Automation, Wuhan University, Wuhan, Hubei 430072, China

Xuhan Wan - School of Electrical Engineering and Automation, Wuhan University, Wuhan, Hubei 430072, China

Anyang Wang - School of Electrical Engineering and Automation, Wuhan University, Wuhan, Hubei 430072, China

Feng Ryan Wang - Departments of Chemical Engineering, University College London, Torrington Place, London WC1E 7JE, UK

Notes

The authors declare no competing financial interests in this work.

ACKNOWLEDGMENTS

REFERENCES

(1) Chu, S.; Majumdar, A., Opportunities and Challenges for a Sustainable Energy Future. *Nature* **2012,** *488*, 294-303.

(2) Seh, Z. W.; Kibsgaard, J.; Dickens, C. F.; Chorkendorff, I.; Nørskov, J. K.; Jaramillo, T. F., Combining Theory and Experiment in Electrocatalysis: Insights into Materials Design. *Science* **2017,** *355*, eaad4998.

(3) Cano, Z. P.; Banham, D.; Ye, S.; Hintennach, A.; Lu, J.; Fowler, M.; Chen, Z., Batteries and Fuel Cells for Emerging Electric Vehicle Markets. *Nat. Energy* **2018,** *3*, 279-289.

(4) Kibsgaard, J.; Chorkendorff, I., Considerations for the Scaling-up of Water Splitting Catalysts. *Nat. Energy* **2019,** *4*, 430-433.

(5) Debe, M. K., Electrocatalyst Approaches and Challenges for Automotive Fuel Cells. *Nature* **2012,** *486*, 43-51.

(6) Zhao, Z.; Li, M.; Zhang, L.; Dai, L.; Xia, Z., Design Principles for Heteroatom‐Doped Carbon Nanomaterials as Highly Efficient Catalysts for Fuel Cells and Metal‐Air Batteries. *Adv. Mater.* **2015,** *27*, 6834-6840.

(7) Zeng, K.; Zheng, X.; Li, C.; Yan, J.; Tian, J. H.; Jin, C.; Strasser, P.; Yang, R., Recent Advances in Non‐Noble Bifunctional Oxygen Electrocatalysts toward Large‐Scale Production. *Adv. Funct. Mater.* **2020,** *30*, 2000503.

(8) Huang, Z. F.; Wang, J.; Peng, Y.; Jung, C. Y.; Fisher, A.; Wang, X., Design of Efficient Bifunctional Oxygen Reduction/Evolution Electrocatalyst: Recent Advances and Perspectives. *Adv. Energy Mater.* **2017,** *7*, 1700544.

(9) Wang, Y.-J.; Wilkinson, D. P.; Zhang, J., Noncarbon Support Materials for Polymer Electrolyte Membrane Fuel Cell Electrocatalysts. *Chem. Rev.* **2011,** *111*, 7625-7651.

(10) Zhang, J.; Zhao, Z.; Xia, Z.; Dai, L., A Metal-Free Bifunctional Electrocatalyst for Oxygen Reduction and Oxygen Evolution Reactions. *Nat. Nanotechnol.* **2015,** *10*, 444-452.

(11) Reier, T.; Oezaslan, M.; Strasser, P., Electrocatalytic Oxygen Evolution Reaction (OER) on Ru, Ir, and Pt Catalysts: A Comparative Study of Nanoparticles and Bulk Materials. *ACS Catal.* **2012,** *2*, 1765-1772.

(12) He, T.; Matta, S. K.; Will, G.; Du, A., Transition-Metal Single Atoms Anchored on Graphdiyne as High-Efficiency Electrocatalysts for Water Splitting and Oxygen Reduction. *Small Methods* **2019,** *3*, 1800419.

(13) Peng, L.; Shang, L.; Zhang, T.; Waterhouse, G. I., Recent Advances in the Development of Single-Atom Catalysts for Oxygen Electrocatalysis and Zinc-Air Batteries. *Adv. Energy Mater.* **2020,** *10*, 2003018.

(14) Qiao, B.; Wang, A.; Yang, X.; Allard, L. F.; Jiang, Z.; Cui, Y.; Liu, J.; Li, J.; Zhang, T., Single-Atom Catalysis of CO Oxidation Using Pt_1/FeO_x. *Nat. Chem.* **2011,** *3*, 634-641.

(15) Fei, H.; Dong, J.; Feng, Y.; Allen, C. S.; Wan, C.; Volosskiy, B.; Li, M.; Zhao, Z.; Wang, Y.; Sun, H., General Synthesis and Definitive Structural Identification of MN_4C_4 Single-Atom Catalysts with Tunable Electrocatalytic Activities. *Nat. Catal.* **2018,** *1*, 63-72.

(16) Xu, H.; Cheng, D.; Cao, D.; Zeng, X. C., A Universal Principle for a Rational Design of Single-Atom Electrocatalysts. *Nat. Catal.* **2018,** *1*, 339-348.

(17) Niu, H.; Wang, X.; Shao, C.; Liu, Y.; Zhang, Z.; Guo, Y., Revealing Oxygen Reduction Reaction Activity Origin of Single Atom Supported on g-C_3N_4 Monolayer: A First-Principles Study. *J. Mater. Chem. A* **2020,** *8*, 6555-6563.

(18) Lv, X.; Wei, W.; Zhao, P.; Er, D.; Huang, B.; Dai, Y.; Jacob, T., Oxygen-Terminated Bixenes and Derived Single Atom Catalysts for the Hydrogen Evolution Reaction. *J. Catal.* **2019,** *378*, 97-103.

(19) Kaiser, S. K.; Chen, Z.; Faust Akl, D.; Mitchell, S.; Pérez-Ramírez, J., Single-Atom Catalysts across the Periodic Table. *Chem. Rev.* **2020,** *120*, 11703-11809.

(20) Niu, H.; Zhang, Z.; Wang, X.; Wan, X.; Shao, C.; Guo, Y., Theoretical Insights into the Mechanism of Selective Nitrate-to-Ammonia Electroreduction on Single-Atom Catalysts. *Adv. Funct. Mater.* **2021,** *31*, 2008533.

(21) Niu, H.; Wan, X.; Wang, X.; Shao, C.; Robertson, J.; Zhang, Z.; Guo, Y., Single-Atom Rhodium on Defective g-C_3N_4: A Promising Bifunctional Oxygen Electrocatalyst. *ACS Sustainable Chem. Eng.* **2021,** *9*, 3590-3599.

(22) Tang, C.; Chen, L.; Li, H.; Li, L.; Jiao, Y.; Zheng, Y.; Xu, H.; Davey, K.; Qiao, S.-Z., Tailoring Acidic Oxygen Reduction Selectivity on Single-Atom Catalysts Via Modification of First and Second Coordination Spheres. *J. Am. Chem. Soc.* **2021,** *143*, 7819-7827.

(23) Yao, Y.; Hu, S.; Chen, W.; Huang, Z.-Q.; Wei, W.; Yao, T.; Liu, R.; Zang, K.; Wang, X.; Wu, G., Engineering the Electronic Structure of Single Atom Ru Sites Via Compressive Strain Boosts Acidic Water Oxidation Electrocatalysis. *Nat. Catal.* **2019,** *2*, 304-313.

(24) Yang, X.-F.; Wang, A.; Qiao, B.; Li, J.; Liu, J.; Zhang, T., Single-Atom Catalysts: A New Frontier in Heterogeneous Catalysis. *Acc. Chem. Res.* **2013,** *46*, 1740-1748.

(25) Liu, J.-C.; Tang, Y.; Wang, Y.-G.; Zhang, T.; Li, J., Theoretical Understanding of the Stability of Single-Atom Catalysts. *Natl. Sci. Rev.* **2018,** *5*, 638-641.

(26) Zhu, Y.; Sun, W.; Luo, J.; Chen, W.; Cao, T.; Zheng, L.; Dong, J.; Zhang, J.; Zhang, M.; Han, Y., A Cocoon Silk Chemistry Strategy to Ultrathin N-Doped Carbon Nanosheet with Metal Single-Site Catalysts. *Nat. Commun.* **2018,** *9*, 1-9.

(27) Du, Z.; Chen, X.; Hu, W.; Chuang, C.; Xie, S.; Hu, A.; Yan, W.; Kong, X.; Wu, X.; Ji, H., Cobalt in Nitrogen-Doped Graphene as Single-Atom Catalyst for High-Sulfur Content Lithium-Sulfur Batteries. *J. Am. Chem. Soc.* **2019,** *141*, 3977-3985.

(28) Liu, J.; Xiao, J.; Luo, B.; Tian, E.; Waterhouse, G. I., Central Metal and Ligand Effects on Oxygen Electrocatalysis over 3d Transition Metal Single-Atom Catalysts: A Theoretical Investigation. *Chem. Eng. J.* **2022,** *427*, 132038.

(29) Liu, X.; Jiao, Y.; Zheng, Y.; Jaroniec, M.; Qiao, S.-Z., Building up a Picture of the Electrocatalytic Nitrogen Reduction Activity of Transition Metal Single Atom Catalysts. *J. Am. Chem. Soc.* **2019,** *141*, 9664-9672.

(30) Zheng, Y.; Jiao, Y.; Zhu, Y.; Cai, Q.; Vasileff, A.; Li, L. H.; Han, Y.; Chen, Y.; Qiao, S.-Z., Molecule-Level g-C_3N_4 Coordinated Transition Metals as a New Class of Electrocatalysts for Oxygen Electrode Reactions. *J. Am. Chem. Soc.* **2017,** *139*, 3336-3339.

(31) Niu, H.; Wang, X.; Shao, C.; Liu, Y.; Zhang, Z.; Guo, Y., Revealing the Oxygen Reduction Reaction Activity Origin of Single Atoms Supported on g-C_3N_4 Monolayers: A First-Principles Study. *J. Mater. Chem. A* **2020,** *8*, 6555-6563.

(32) Anasori, B.; Lukatskaya, M. R.; Gogotsi, Y., 2D Metal Carbides and Nitrides (Mxenes) for Energy Storage. *Nature Reviews Materials* **2017,** *2*, 1-17.

(33) Peng, Q.; Zhou, J.; Chen, J.; Zhang, T.; Sun, Z., Cu Single Atoms on Ti_2CO_2 as a Highly Efficient Oxygen Reduction Catalyst in a Proton Exchange Membrane Fuel Cell. *J. Mater. Chem. A* **2019,** *7*, 26062-26070.

(34) Deng, J.; Li, H.; Xiao, J.; Tu, Y.; Deng, D.; Yang, H.; Tian, H.; Li, J.; Ren, P.; Bao, X., Triggering the Electrocatalytic Hydrogen Evolution Activity of the Inert Two-Dimensional MoS_2 Surface Via Single-Atom Metal Doping. *Energy Environ. Sci.* **2015,** *8*, 1594-1601.

(35) Guo, H.; Li, L.; Wang, X.; Yao, G.; Yu, H.; Tian, Z.; Li, B.; Chen, L., Theoretical Investigation on the Single Transition-Metal Atom-Decorated Defective MoS_2 for Electrocatalytic Ammonia Synthesis. *ACS Appl. Mater. Interfaces* **2019,** *11*, 36506-36514.

(36) Chung, H. T.; Cullen, D. A.; Higgins, D.; Sneed, B. T.; Holby, E. F.; More, K. L.; Zelenay, P., Direct Atomic-Level Insight into the Active Sites of a High-Performance Pgm-Free ORR Catalyst. *Science* **2017,** *357*, 479-484.

(37) Chen, Y.; Ji, S.; Zhao, S.; Chen, W.; Dong, J.; Cheong, W.-C.; Shen, R.; Wen, X.; Zheng, L.; Rykov, A. I., Enhanced Oxygen Reduction with Single-Atomic-Site Iron Catalysts for a Zinc-Air Battery and Hydrogen-Air Fuel Cell. *Nat. Commun.* **2018,** *9*, 1-12.

(38) Jiang, W.-J.; Gu, L.; Li, L.; Zhang, Y.; Zhang, X.; Zhang, L.-J.; Wang, J.-Q.; Hu, J.-S.; Wei, Z.; Wan, L.-J., Understanding the High Activity of Fe-N-C Electrocatalysts in Oxygen Reduction: Fe/Fe_3C Nanoparticles Boost the Activity of Fe-N_x. *J. Am. Chem. Soc.* **2016,** *138*, 3570-3578.

(39) Mahmood, J.; Lee, E. K.; Jung, M.; Shin, D.; Choi, H.-J.; Seo, J.-M.; Jung, S.-M.; Kim, D.; Li, F.; Lah, M. S., Two-Dimensional Polyaniline (C_3N) from Carbonized Organic Single Crystals in Solid State. *Proc. Natl. Acad. Sci.* **2016,** *113*, 7414-7419.

(40) Mortazavi, B., Ultra High Stiffness and Thermal Conductivity of Graphene Like C_3N. *Carbon* **2017,** *118*, 25-34.

(41) Bafekry, A.; Farjami Shayesteh, S.; Peeters, F. M., C_3N Monolayer: Exploring the Emerging of Novel Electronic and Magnetic Properties with Adatom Adsorption, Functionalizations, Electric Field, Charging, and Strain. *J. Phys. Chem. C* **2019,** *123*, 12485-12499.

(42) Xu, J.; Mahmood, J.; Dou, Y.; Dou, S.; Li, F.; Dai, L.; Baek, J. B., 2D Frameworks of C_2N and C_3N as New Anode Materials for Lithium-Ion Batteries. *Adv. Mater.* **2017,** *29*, 1702007.

(43) Ma, D.; Zhang, J.; Li, X.; He, C.; Lu, Z.; Lu, Z.; Yang, Z.; Wang, Y., C_3N Monolayers as Promising Candidates for NO_2 Sensors. *Sens. Actuators, B* **2018,** *266*, 664-673.

(44) Li, X.; Guo, T.; Zhu, L.; Ling, C.; Xue, Q.; Xing, W., Charge-Modulated CO_2 Capture of C_3N Nanosheet: Insights from DFT Calculations. *Chem. Eng. J.* **2018,** *338*,

92-98.

(45) Zhao, Y.; Ma, D.; Zhang, J.; Lu, Z.; Wang, Y., Transition Metal Embedded C_3N Monolayers as Promising Catalysts for the Hydrogen Evolution Reaction. *Phys. Chem. Chem. Phys.* **2019,** *21*, 20432-20441.

(46) Zhou, Y.; Gao, G.; Kang, J.; Chu, W.; Wang, L.-W., Transition Metal-Embedded Two-Dimensional C_3N as a Highly Active Electrocatalyst for Oxygen Evolution and Reduction Reactions. *J. Mater. Chem. A* **2019,** *7*, 12050-12059.

(47) Nong, W.; Qin, S.; Huang, F.; Liang, H.; Yang, Z.; Qi, C.; Li, Y.; Wang, C., Designing C_3N-Supported Single Atom Catalysts for Efficient Nitrogen Reduction Based on Descriptor of Catalytic Activity. *Carbon* **2021,** *182*, 297-306.

(48) Kresse, G.; Furthmüller, J., Efficient Iterative Schemes for Ab Initio Total-Energy Calculations Using a Plane-Wave Basis Set. *Phys. Rev. B* **1996,** *54*, 11169.

(49) Perdew, J. P.; Burke, K.; Ernzerhof, M., Generalized Gradient Approximation Made Simple. *Phys. Rev. Lett.* **1996,** *77*, 3865.

(50) Heyd, J.; Scuseria, G. E.; Ernzerhof, M., Hybrid Functionals Based on a Screened Coulomb Potential. *J. Chem. Phys.* **2003,** *118*, 8207-8215.

(51) Grimme, S., Semiempirical GGA-Type Density Functional Constructed with a Long-Range Dispersion Correction. *J. Comput. Chem.* **2006,** *27*, 1787-1799.

(52) Mathew, K.; Sundararaman, R.; Letchworth-Weaver, K.; Arias, T.; Hennig, R. G., Implicit Solvation Model for Density-Functional Study of Nanocrystal Surfaces and Reaction Pathways. *J. Chem. Phys.* **2014,** *140*, 084106.

(53) Henkelman, G.; Uberuaga, B. P.; Jónsson, H., A Climbing Image Nudged Elastic Band Method for Finding Saddle Points and Minimum Energy Paths. *J. Chem. Phys.* **2000,** *113*, 9901-9904.

(54) Nørskov, J. K.; Rossmeisl, J.; Logadottir, A.; Lindqvist, L.; Kitchin, J. R.; Bligaard, T.; Jónsson, H., Origin of the Overpotential for Oxygen Reduction at a Fuel-Cell Cathode. *J. Phys. Chem. B* **2004,** *108*, 17886-17892.

(55) Nørskov, J. K.; Bligaard, T.; Logadottir, A.; Kitchin, J.; Chen, J. G.; Pandelov, S.; Stimming, U., Trends in the Exchange Current for Hydrogen Evolution. *J. Electrochem. Soc.* **2005,** *152*, J23-J26.

(56) Guo, X.; Gu, J.; Lin, S.; Zhang, S.; Chen, Z.; Huang, S., Tackling the Activity and Selectivity Challenges of Electrocatalysts toward the Nitrogen Reduction Reaction Via Atomically Dispersed Biatom Catalysts. *J. Am. Chem. Soc.* **2020,** *142*, 5709-5721.

(57) Zhang, X.; Chen, A.; Zhang, Z.; Jiao, M.; Zhou, Z., Transition Metal Anchored C_2N Monolayers as Efficient Bifunctional Electrocatalysts for Hydrogen and Oxygen Evolution Reactions. *J. Mater. Chem. A* **2018,** *6*, 11446-11452.

(58) Makaremi, M.; Mortazavi, B.; Singh, C. V., Adsorption of Metallic, Metalloidic, and Nonmetallic Adatoms on Two-Dimensional C_3N. *J. Phys. Chem. C* **2017,** *121*, 18575-18583.

(59) Man, I. C.; Su, H. Y.; Calle-Vallejo, F.; Hansen, H. A.; Martínez, J. I.; Inoglu, N. G.; Kitchin, J.; Jaramillo, T. F.; Nørskov, J. K.; Rossmeisl, J., Universality in Oxygen Evolution Electrocatalysis on Oxide Surfaces. *ChemCatChem* **2011,** *3*, 1159-1165.

(60) Medford, A. J.; Vojvodic, A.; Hummelshøj, J. S.; Voss, J.; Abild-Pedersen, F.; Studt, F.; Bligaard, T.; Nilsson, A.; Nørskov, J. K., From the Sabatier Principle to a Predictive

Theory of Transition-Metal Heterogeneous Catalysis. *J. Catal.* **2015,** *328*, 36-42.

(61) Jiao, Y.; Zheng, Y.; Jaroniec, M.; Qiao, S. Z., Design of Electrocatalysts for Oxygen-and Hydrogen-Involving Energy Conversion Reactions. *Chem. Soc. Rev.* **2015,** *44*, 2060-2086.

(62) Wei, B.; Fu, Z.; Legut, D.; Germann, T. C.; Du, S.; Zhang, H.; Francisco, J. S.; Zhang, R., Rational Design of Highly Stable and Active Mxene-Based Bifunctional ORR/OER Double-Atom Catalysts. *Adv. Mater.* **2021,** *33*, 2102595.

(63) Zhou, Y.; Sheng, L.; Luo, Q.; Zhang, W.; Yang, J., Improving the Activity of Electrocatalysts toward the Hydrogen Evolution Reaction, the Oxygen Evolution Reaction, and the Oxygen Reduction Reaction Via Modification of Metal and Ligand of Conductive Two-Dimensional Metal-Organic Frameworks. *J. Phys. Chem. L* **2021,** *12*, 11652-11658.

(64) Nong, W.; Qin, S.; Huang, F.; Liang, H.; Yang, Z.; Qi, C.; Li, Y.; Wang, C., Design C_3N-Supported Single Atom Catalysts for Efficient Nitrogen Reduction Based on Descriptor of Catalytic Activity. *Carbon* **2021**, 297-306.

(65) Gao, W.; Chen, Y.; Li, B.; Liu, S.-P.; Liu, X.; Jiang, Q., Determining the Adsorption Energies of Small Molecules with the Intrinsic Properties of Adsorbates and Substrates. *Nat. Commun.* **2020,** *11*, 1-11.

For Table of Contents Use Only
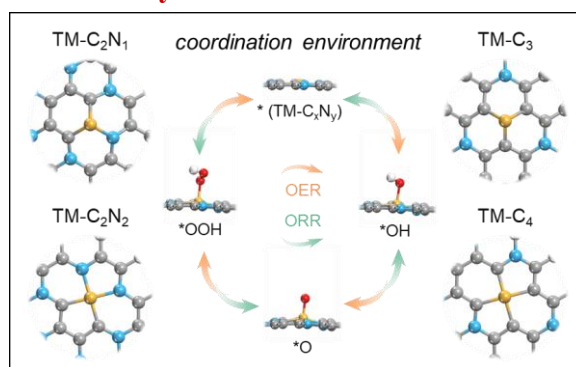
Synopsis

The feasibility of single-atom-embedded C_3N with the various coordination environments of TM-C_xN_y is evaluated for oxygen electrocatalysis.